



PAPER

OPEN ACCESS

RECEIVED
25 November 2019REVISED
7 May 2020ACCEPTED FOR PUBLICATION
18 May 2020PUBLISHED
1 July 2020

Original content from this work may be used under the terms of the [Creative Commons Attribution 4.0 licence](https://creativecommons.org/licenses/by/4.0/).

Any further distribution of this work must maintain attribution to the author(s) and the title of the work, journal citation and DOI.



30 GHz bandwidth temperature stable 980 nm vertical-cavity surface-emitting lasers with AlAs/GaAs bottom distributed Bragg reflectors for optical data communication

M Gębski^{1,2}, P -S Wong³, M Riazat³ and J A Lott¹¹ Technische Universität Berlin, Institute of Solid-State Physics, Berlin, Germany² Institute of Physics, Lodz University of Technology, Photonics Group, Łódź, Poland³ OEpic Semiconductors Inc., 1231 Bordeaux Drive, Sunnyvale, California 94089, United States of AmericaE-mail: marcin.gebski@p.lodz.pl**Keywords:** vertical-cavity surface-emitting lasers, optical interconnects, optical data communication

Abstract

We present a 980 nm vertical-cavity surface-emitting laser (VCSEL) design which achieves 32 GHz small-signal modulation bandwidth ($f_{3\text{dB}}$) at 15 °C and record-high 27 GHz at 85 °C. Our devices utilize binary AlAs/GaAs bottom distributed Bragg reflector material layers to improve thermal conductance. We extract key VCSEL figures-of-merit from static optical output power-current-voltage (LIV), spectral emission, and high frequency dynamic measurements and observe highly temperature stable performance for these parameters.

1. Introduction

The estimated number of Internet users grew from 2.4 billion in 2014 to about 4.4 billion by June 2019, an 83% increase in the past roughly 5 years [1]. The amount of data transiting the Internet each day is quite difficult to accurately track but is estimated to be about 2.5 exabytes (10^{18} bytes) [1]. In addition to exponential increases in the use of email, social media, and search requests there is also a shockingly high growth rate in the use of gadgets associated with the Internet of Things concept and due to a plethora of emerging data generating devices. The global Internet Protocol traffic reached ~ 1.1 zettabytes (10^{21} bytes) for all of 2017 and is expected to double from about 200 exabytes per month now to well over 400 exabytes per month by 2023 [2]. The global network of optical interconnects (OIs) is the often invisible yet ubiquitous arteries and veins through which information is sent and received. The distributed hearts and brains of our modern Internet and our data analysis, modeling, and forecasting centers include hundreds of thousands of data centers. Moreover, there are about 500 hyperscale data centers as of 2019 (i.e. data centers with more than 5000 servers with facilities exceeding 10 000 square feet) focused on cloud and Internet services [3], up from about 200 hyperscale centers in 2013. Additionally, there are surely thousands of high performance computers (HPCs) and computer clusters operating as HPCs, for which a list of the running top 500 supercomputers may be accessed via [4]. Semiconductor edge-emitting lasers emitting at ~ 1300 and 1550 nm are the main light sources in OIs for long distance (>1 km) optical telecommunication while for short reach distances (<1 km) the OIs used in data centers and in HPCs employ vertical-cavity surface-emitting lasers (VCSELs) emitting at 850 nm. At very short distances (<1 m) data communication is still realized mostly through relatively slow and inefficient electrical wires [5]. Energy consumption in United States data centers was reportedly about 70 billion kW-hr for 2014 [6, 7] and roughly 90 billion kW-hr for 2017 [8]. Modern data centers consume about 2% of the global supply of electricity and this is expected to increase to 8% by 2030 [2].

Thanks to huge improvements in CMOS transistor technology, only ~ 100 fJ bit⁻¹ is consumed for actual computing (floating point operations) while ~ 600 fJ bit⁻¹ is used for across-chip communication and $\sim 1\text{--}20$ pJ bit⁻¹ is used to communicate off-chip [5]. Even more energy is used to send information (via electrical wires) within microprocessors, and for chip-to-chip, board-to-board, and rack-to-rack. If the ever-growing demand for information transfer is to be satisfied, the short reach OIs will have to become

faster and more energy efficient. Additionally, very short reach (<1 m) OIs will have to be implemented very soon to realize energy efficient and fast board-to-board and chip-to-chip optical communication. It is predicted that in 2022 the energy consumption per bit for both off-chip and on-chip OIs should go below 100 and 10 fJ bit⁻¹ [9]. Due to the fact that the operating temperatures of electronics in data centers can reach 85 °C, the emitters in OIs should not only be fast and energy efficient but also should be characterized by a high temperature stability in a wide range of temperatures up to 85 °C. Thanks to inherently low threshold currents and small mode volumes resulting in high energy efficiency and high modulation bit rates, respectively, VCSELs fulfill these requirements in state-of-the-art short-reach OIs. Thanks to constant development, VCSELs have a high probability to also fulfill the requirements of the OIs of future.

Great improvements in both the high-speed modulation capabilities and energy efficiency of the 850 nm VCSELs that are typically used in OIs were made during the last decade. Numerous groups and companies have presented error free data transmission rates exceeding 50 Gbit s⁻¹ at 25 °C via the simple two-voltage-level, non-return to zero (NRZ) coding scheme [10–15]. For our purposes we define error free transmission as a bit error ratio $< 10^{-12}$. Chalmers University in cooperation with IBM achieved 71 Gbit s⁻¹ error free data transmission speed at 25 °C [16] using a packaged 850 nm VCSEL and special conditioning of the VCSEL drive signal. Furthermore, an error free bit rate of 50 Gbit s⁻¹ at 85 °C was reported for data transmission without any signal conditioning [12, 17]. The highest reported error free bit rate where the energy efficiency was < 100 fJ bit⁻¹ is 50 Gbit s⁻¹ at 25 °C [11], whereas the best reported energy efficiency for all VCSELs is 56 fJ bit⁻¹ for data transmission at 25 Gb s⁻¹ at 25 °C [18].

Very interesting alternatives to 850 nm VCSELs for optical data communication include 940, 980, and 1060 nm VCSELs. Thanks to the new OM5 multiple mode optical fiber where the optical fiber characteristics at 940 nm are identical to the performance characteristics at 850 nm, the 940 nm VCSELs with the smaller energy bandgap in the active region have an intrinsically lower operating voltage and thus potentially enhanced energy efficiency compared to 850 nm VCSELs. Similar arguments may be applied to 980 nm and 1060 nm VCSELs, especially if optical fiber tuned to these specific wavelengths is employed and if the VCSELs emit in a single fundamental LP01 optical mode. Our group over the last 5 years has focused on improving the dynamic properties of 980 nm VCSELs in back-to-back data transmission test set ups (across half-meter OM3 patch cords for example). We have demonstrated error free 38 Gbit s⁻¹ with energy efficiencies of 197 and 177 fJ bit⁻¹ at 25 and 85 °C, respectively [19], 42 Gbit s⁻¹ with an energy efficiency of 217 fJ bit⁻¹ at 25 °C [19], and 139 fJ bit⁻¹ at 35 Gbit s⁻¹ at 85 °C [20]. We further achieved 50 and 52 Gbit s⁻¹ error free data transmission at 25 °C and 46 and 50 Gbit s⁻¹ at 85 °C, respectively [21, 22]. 31 GHz bandwidth at 25 °C and 25 GHz bandwidth at 85 °C was reported in [23]. The highest bandwidth reported to date for a 980 nm VCSEL is 35.5 GHz at 25 °C [24, 25]. A review of the advances in VCSELs for data communication can be found in [26].

In this paper we present the design and characterization of a simplified epitaxial design of a 980 nm VCSEL (compared to those designs reported in our previous work cited above) where we incorporate a hybrid bottom distributed Bragg reflector (DBR) mirror composed of both AlAs/GaAs and AlGaAs/GaAs DBR sections for better heat dissipation and show the impact of this design on the measured VCSEL performance figures-of-merit. In section 1 we explain the details of the epitaxial structure and our processing methods. In sections 2.1 and 2.2 we present and analyze the static and dynamic properties of our devices, respectively. In section 3 we conclude our work.

2. Methods

2.1. Epitaxial structure

The VCSEL wafers are grown by metal-organic vapor-phase epitaxy (MOVPE) on semi-insulating 001-surface-oriented GaAs substrates. We illustrate the complete epitaxial structure via the cross-section schematic in figure 1(a). The 200 nm-thick (n+)GaAs initial buffer layer is followed by a half-lambda optically-thick In_{0.5}Ga_{0.5}P layer lattice-matched to GaAs followed in turn by an ~ 1.586 μm -thick (n+)GaAs ohmic contact/current spreading layer. Next, we grow the bottom Si-doped distributed Bragg reflector (DBR) mirror which consists of a 33 period binary AlAs/GaAs DBR plus a 3 period GaAs/Al_{0.9}Ga_{0.1}As DBR between the binary DBR and the optical cavity active region. Both bottom DBR sections use linearly compositionally graded regions from $x = 0.0$ to 0.90 or from $x = 0.0$ to 1.0, and vice versa over a thickness of 18 nm. The two low refractive index DBR layers that are adjacent to the half-lambda optically thick optical cavity include 20 nm-thick (as grown) Al_{0.98}Ga_{0.02}As layers that are subsequently selectively thermally oxidized during the device processing in order to form an electrical aperture. The top 18.5 period C-doped DBR consists of GaAs/Al_{0.9}Ga_{0.1}As with linearly compositionally graded interfaces, also each over a thickness of 18 nm. Five compressively strained 4.2 nm-thick In_yGa_{1-y}As ($y \sim 0.23$) quantum wells (QWs) are centered in the optical cavity and surrounded by undoped 6.0 nm-thick GaAs_{0.84}P_{0.16} barrier layers.

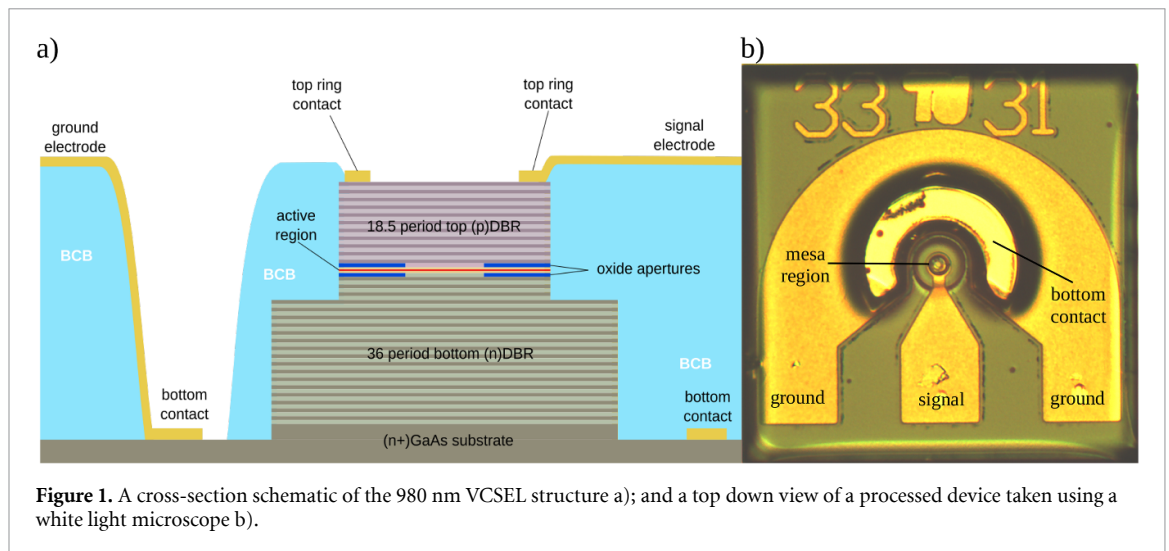


Figure 1. A cross-section schematic of the 980 nm VCSEL structure a); and a top down view of a processed device taken using a white light microscope b).

2.2. Processing

We process the VCSELs using planar processing techniques developed at the Technical University Berlin (TUB). In the first step, the top ring p-metal contact patterns are defined by ultraviolet (UV) contact lithography followed by the deposition of Ti/Pt/Au via electron beam evaporation and photoresist lift-off. Next the top mesa patterns are defined using UV lithography and dry-etched in BCl_3 -based plasma in an inductively coupled plasma reactive ion etching (ICP-RIE) reactor. The etching is stopped after the optical cavity plus the first 2.5 periods of the GaAs/ $\text{Al}_{0.9}\text{Ga}_{0.1}\text{As}$ bottom DBR. We thus etch down past the two $\text{Al}_{0.98}\text{Ga}_{0.02}\text{As}$ layers and stop before reaching the first AlAs layer in the bottom GaAs/AlAs DBR. In the next device processing step, we perform a selective wet thermal oxidation of the Al-rich layers in a purified de-ionized water vapor environment at 420°C and at 50 mbar to form the two oxide aperture layers. To enhance heatsinking of the structure second second (bottom) mesas of a large diameter are patterned using UV contact photolithography. We then dry-etch the second mesas in a process similar to the first mesa etching. We stop the dry etching a short, arbitrary depth into the $\sim 1.586\ \mu\text{m}$ thick (n+)GaAs ohmic contact/current spreading layer after etching through the entire bottom DBR including of course the entire lower AlAs/GaAs DBR section. Next, the bottom Ni/AuGe/Au n-type contacts are patterned using UV contact photolithography and deposited using a thermal metal evaporator. To lower the contact resistance of the n-type contacts, the structures are annealed in a rapid thermal annealing (RTA) reactor for 1 min in a saturated nitrogen gas atmosphere at 420°C . The wafer pieces are then planarized using a standard benzocyclobutene (BCB) spin-on photosensitive polymer. The BCB layer is then patterned to expose the top mesas and the top p-metal ring contacts and also the bottom n-metal contacts. In the final step, high-speed, Ti/Pt/Au ground-signal-ground (GSG) co-planar electrodes are patterned using UV contact photolithography and deposited using an electron-beam metal evaporator. The resulting VCSELs have top mesa diameters ranging from 18 to $31\ \mu\text{m}$ and oxide aperture diameters ranging from 4 to $17\ \mu\text{m}$. In figure 1(b) we show a microscope image of an example fully processed VCSEL.

3. Results

3.1. Static measurements

We performed static optical output power-current-voltage (*LIV*) and spectral emission measurements for five devices with oxide aperture diameters of ~ 4 to $6\ \mu\text{m}$ in steps of $0.5\ \mu\text{m}$ and corresponding top mesa diameters of 18 to $20\ \mu\text{m}$, also in steps of $0.5\ \mu\text{m}$. The five VCSELs are adjacent lasers in one column with a vertical center-to-center pitch of $600\ \mu\text{m}$. We assume that the non-uniformity in the VCSEL layer compositions for this set of VCSELs is negligible. The VCSELs are tested on wafer using a standard high frequency ground-signal-ground (GSG) probe with a needle contact spacing of $150\ \mu\text{m}$. The entire wafer piece (with a physical size of $\sim 10\ \text{mm} \times 20\ \text{mm}$) is placed on a copper plate that serves as a heatsink without using heat conducting paste. We vary the heatsink temperatures from 15 to 85°C in 10°C steps. In the case of the *LIV* measurements the output optical power is collected by an integration sphere with an InGaAs photodetector. The photodetector current is measured by a current meter and converted to optical power at 980 nm via a known responsivity (A/W). In the case of the spectral emission measurements, the output optical signal is coupled into a standard OM1 multiple mode silica fiber with a fiber core diameter of

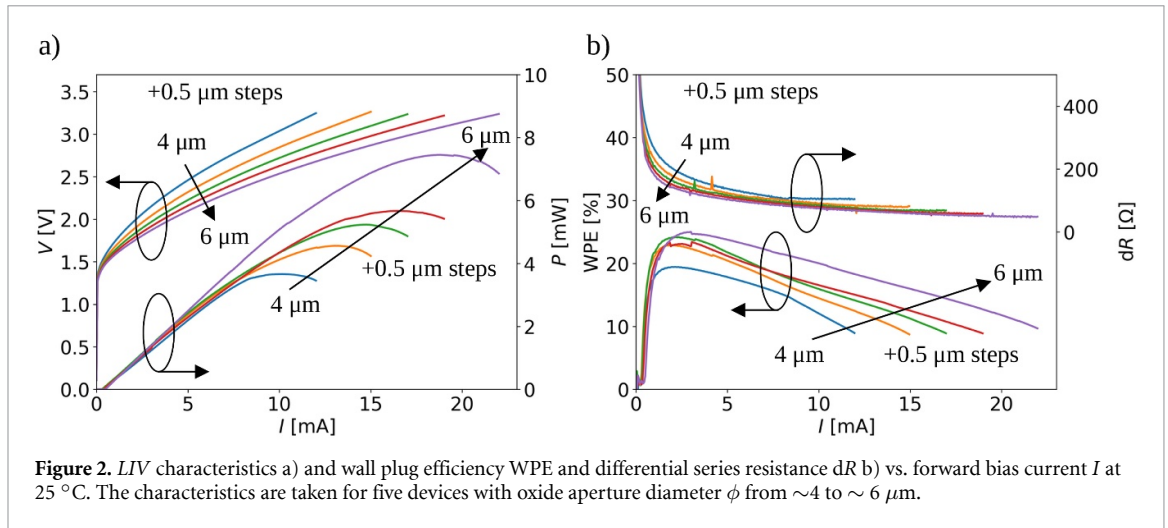


Figure 2. *LIV* characteristics a) and wall plug efficiency WPE and differential series resistance dR b) vs. forward bias current I at 25 °C. The characteristics are taken for five devices with oxide aperture diameter ϕ from ~ 4 to $\sim 6 \mu\text{m}$.

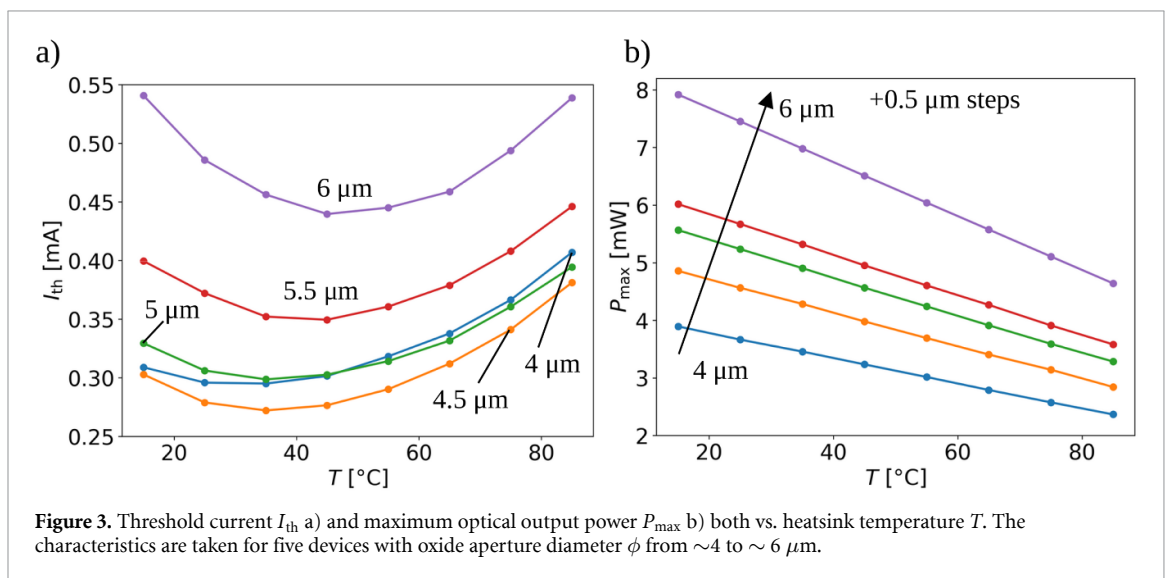


Figure 3. Threshold current I_{th} a) and maximum optical output power P_{max} b) both vs. heatsink temperature T . The characteristics are taken for five devices with oxide aperture diameter ϕ from ~ 4 to $\sim 6 \mu\text{m}$.

62.5 μm and directed into an Ando AQ6317 C optical spectrum analyzer. All the spectra were measured with 0.02 nm resolution and a sensitivity setting which resulted in noise levels down to -70 dBm.

Example *LIV* characteristics taken at 25 °C for the five VCSELs are presented in figure 2(a). From the *LIV* measurements we extract the threshold currents and maximal optical output powers at rollover which depend on temperature. This data is presented in figures 3(a) and (b), respectively. The minimum and maximum threshold currents for the five devices are in the range of 0.27 to 0.55 mA at all temperatures from 15 to 85 °C. The minimum of the threshold current is located between 35 and 45 °C and generally increases in temperature as ϕ increases, as can be seen in figure 3(b). This minimum at a given temperature is an indication of a zero etalon-to-gain detuning at that temperature and as a consequence we determine that we have a negative etalon-to-gain peak wavelength detuning at RT (room temperature) in the range from -7 to -8 nm. The maximum optical output power (P_{max}) changes linearly from 3.9 to 2.4 mW at 15 and 85 °C, respectively for the VCSEL with $\phi \sim 4.0 \mu\text{m}$. For the VCSEL with $\phi \sim 6.0 \mu\text{m}$ the P_{max} changes also linearly but from 7.9 to 4.6 mW at 15 and 85 °C, respectively.

From the *LIV* measurements we extract the differential resistance (dR) defined as dV/dI and the wall plug efficiency (WPE) defined as L/VI . We plot the dR and WPE in figure 2(b). As can be seen in figure 2(b), in order to obtain the best WPE, the optimal current bias working point is located only few milliamperes above the threshold current for all five devices. For increasing bias current, the WPE decreases. On the other hand, for low dR it is better to operate at higher currents because dR always decreases with increasing bias current.

The WPE and dR extracted at two different working points—at the *LI* rollover and at the maximal WPE, are plotted versus heatsink temperature in figures 4 and 5, respectively. As one can see, at the *LI* rollover the WPE varies between 11 and 13.5% for all five devices and is reasonably stable with respect to temperature while dR varies from 50 Ω (for $\phi \sim 6 \mu\text{m}$) to 110 Ω (for $\phi \sim 4 \mu\text{m}$) and is increasing with increasing temperature by $\sim 10\%$ for all devices. On the other hand, the maximum WPE ranges from 17.5% to 25.5%

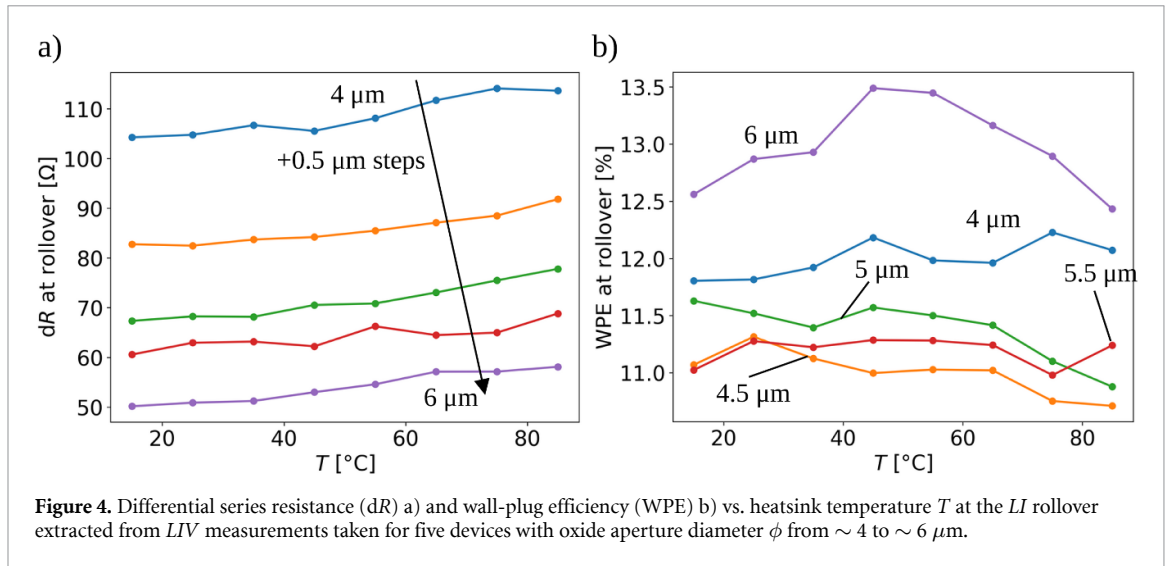


Figure 4. Differential series resistance (dR) a) and wall-plug efficiency (WPE) b) vs. heatsink temperature T at the LI rollover extracted from LIV measurements taken for five devices with oxide aperture diameter ϕ from ~ 4 to ~ 6 μm .

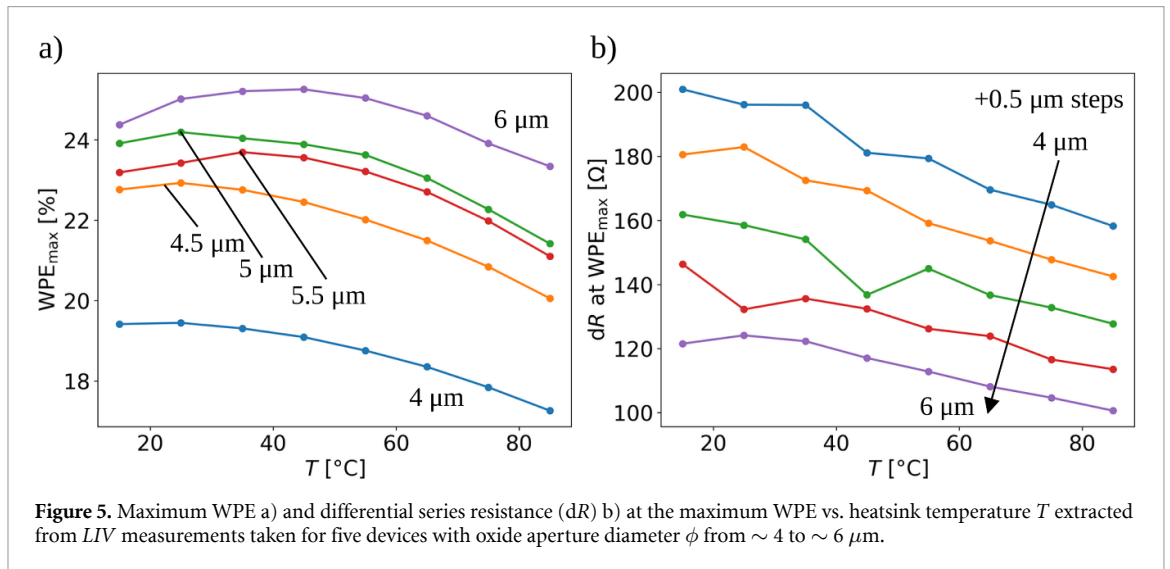


Figure 5. Maximum WPE a) and differential series resistance (dR) b) at the maximum WPE vs. heatsink temperature T extracted from LIV measurements taken for five devices with oxide aperture diameter ϕ from ~ 4 to ~ 6 μm .

for all five devices and decreases by $\sim 10\%$ with a temperature increase from 15 to 85 °C. The dR at maximum WPE ranges from 120 Ω (for $\phi \sim 6$ μm) to 200 Ω (for $\phi \sim 4$ μm) and decreases by $\sim 20\%$ with a temperature increase from 15 to 85 °C.

Example emission spectra for the $\phi \sim 4$ μm VCSEL taken at 25 °C for different currents above the threshold are shown in figure 6(a). The device emits in a single transverse mode from threshold up to 7 mA with a side-mode suppression ratio (SMSR) of at least 40 dB. Similar spectra are taken for all five VCSELs at temperatures from 15 to 85 °C in 10 °C steps. The fundamental mode LP₀₁ peak emission wavelengths for currents from threshold to the LI rollover are extracted from the spectra. The peak emission wavelength for fixed current right above the thresholds (at $I = 1$ mA) is a linear function of the temperature. The slopes of this function ($d\lambda/dT$) are calculated for all five devices by a linear fit. Additionally, the peak emission wavelength for fixed temperature is also a linear function of dissipated power (P_{diss}) defined as the electrical power IV minus the optical output power P taken at the same bias current. The slopes of this function ($d\lambda/dP_{\text{diss}}$) are calculated for all five devices by a linear fit for temperatures from 15 to 85 °C in 10 °C steps. Finally, having the two slopes, the thermal resistance ($R_T = (d\lambda/dP_{\text{diss}})/(d\lambda/dT)$) is calculated for all five devices for temperatures from 15 to 85 °C in 10 °C steps. The thermal resistance versus temperature is presented in the figure 6(b). The R_T increases with temperature for all five devices and at 15 and 85 °C is equal to 3.25 and 3.95 K mW⁻¹ respectively for the $\phi \sim 4$ μm VCSEL and 2.17 and 2.60 K mW⁻¹ respectively for the $\phi \sim 6$ μm VCSEL. The average relative increase of the R_T for all five devices equals 28%.

3.2. Dynamic measurements

The dynamic characteristics of the VCSELs are evaluated based on the standard single-mode laser diode rate-equations model [27]. The standard small-signal frequency response measurement experiment

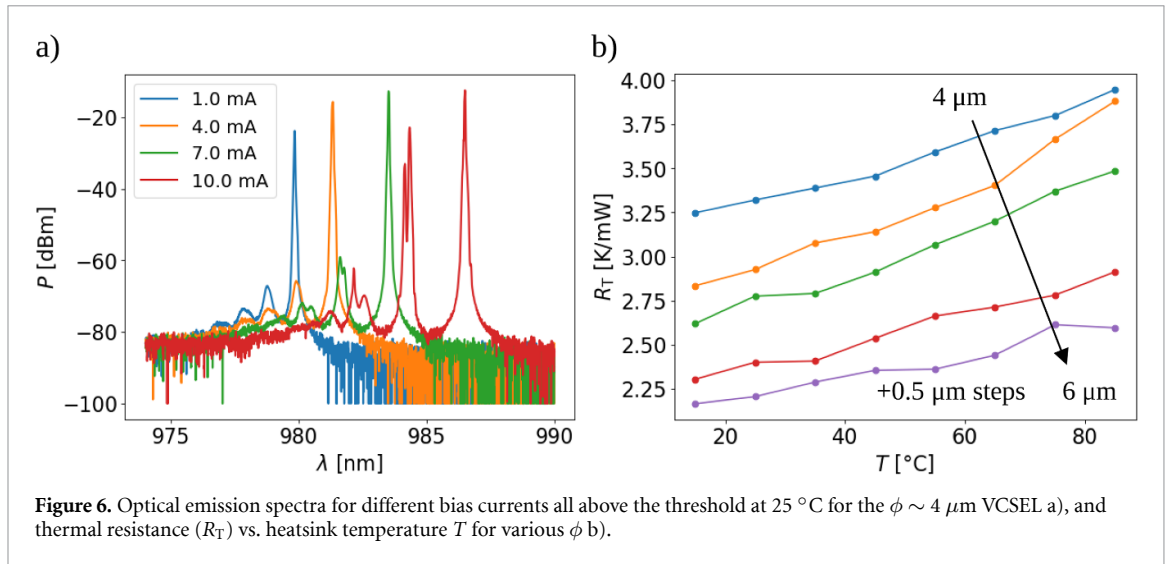


Figure 6. Optical emission spectra for different bias currents all above the threshold at 25 °C for the $\phi \sim 4 \mu\text{m}$ VCSEL a), and thermal resistance (R_T) vs. heatsink temperature T for various ϕ b).

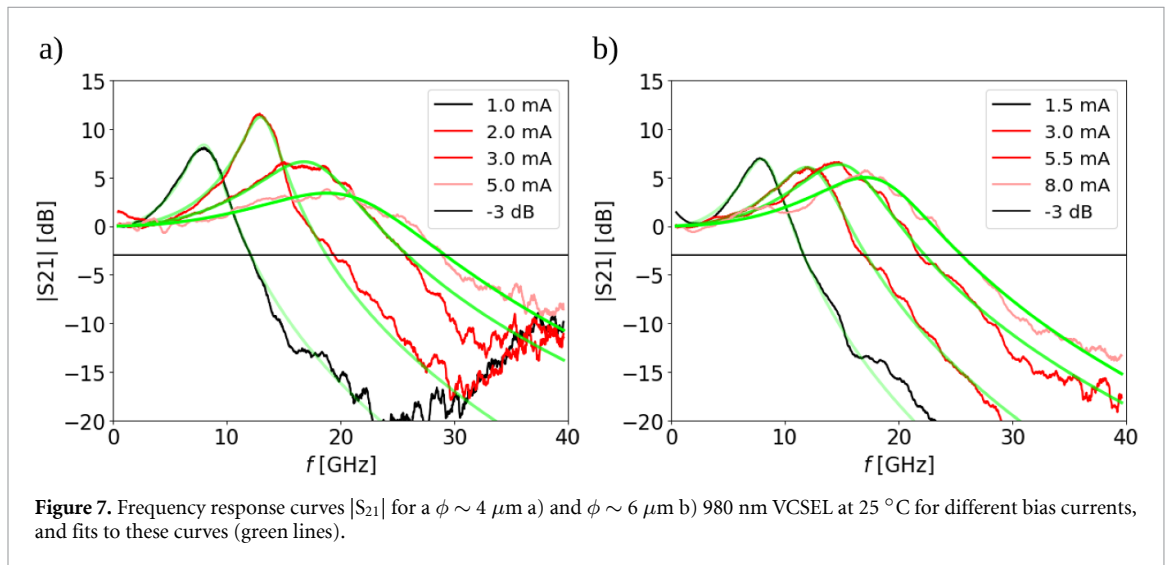


Figure 7. Frequency response curves $|S_{21}|$ for a $\phi \sim 4 \mu\text{m}$ a) and $\phi \sim 6 \mu\text{m}$ b) 980 nm VCSEL at 25 °C for different bias currents, and fits to these curves (green lines).

conducted with the use of a vector network analyzer (VNA) gives us response curves ($|S_{21}|$) of a system composed of a VCSEL, which is sending an optical signal via a silica multi-mode optical fiber (MMF) patch cord, to a high-speed photodetector at a given VCSEL bias current. The figures-of-merit which are extracted from the fit of the $|S_{21}|$ curves to a standard two-pole transfer function are the bandwidth ($f_{3\text{dB}}$), the damping (γ), the parasitic frequency (f_p), and the relaxation oscillation resonance frequency (f_r). The detailed description of the method and the measurement setup can be found in Supplement A at the end of this paper.

An example of an $|S_{21}|$ measurement performed at 25 °C on a $\phi \sim 4$ and $\phi \sim 6 \mu\text{m}$ 980 nm VCSEL for different bias currents above the threshold is presented in figure 7. Similar measurements were performed for all five devices at temperatures from 15 to 85 °C in 10 °C steps and at bias currents from threshold to the LI rollover in 0.1 mA steps.

Examples plots of $f_{3\text{dB}}$ vs. bias current at 25 °C for all five devices and $f_{3\text{dB}}$ vs. bias current for the $\phi \sim 4 \mu\text{m}$ VCSEL at temperatures from 25 to 85 °C with 20 °C steps are presented in figures 8(a) and 9(a), respectively. By fitting the linear part of the f_r versus $\sqrt{(I - I_{\text{th}})}$ plot the D-factors are determined. Examples of such curve fitting at 25 °C for all five devices and for the $\phi \sim 4 \mu\text{m}$ VCSEL at temperatures from 25 to 85 °C with 20 °C step are presented in figures 8(b) and 9(b), respectively.

The evolution of the D-factor with temperature is presented in figure 10(a). The D-factor ranges from 8.1 GHz/ $\sqrt{\text{mA}}$ for the $\phi \sim 6 \mu\text{m}$ VCSEL to 10.8 GHz/ $\sqrt{\text{mA}}$ for the $\phi \sim 4 \mu\text{m}$ VCSEL at 15 °C and from 8.9 GHz/ $\sqrt{\text{mA}}$ for the $\phi \sim 6 \mu\text{m}$ VCSEL to 10.7 GHz/ $\sqrt{\text{mA}}$ for the $\phi \sim 4 \mu\text{m}$ VCSEL at 85 °C. The maximal D-factor is 11.1 GHz/ $\sqrt{\text{mA}}$ for the 4 μm oxide aperture diameter device and it was measured at 25 °C. The D-factor is very stable for all five devices in the full range of temperatures with only slightly pronounced maxima. The small oxide aperture diameter devices tend to have the D-factor maxima at lower heat-sink

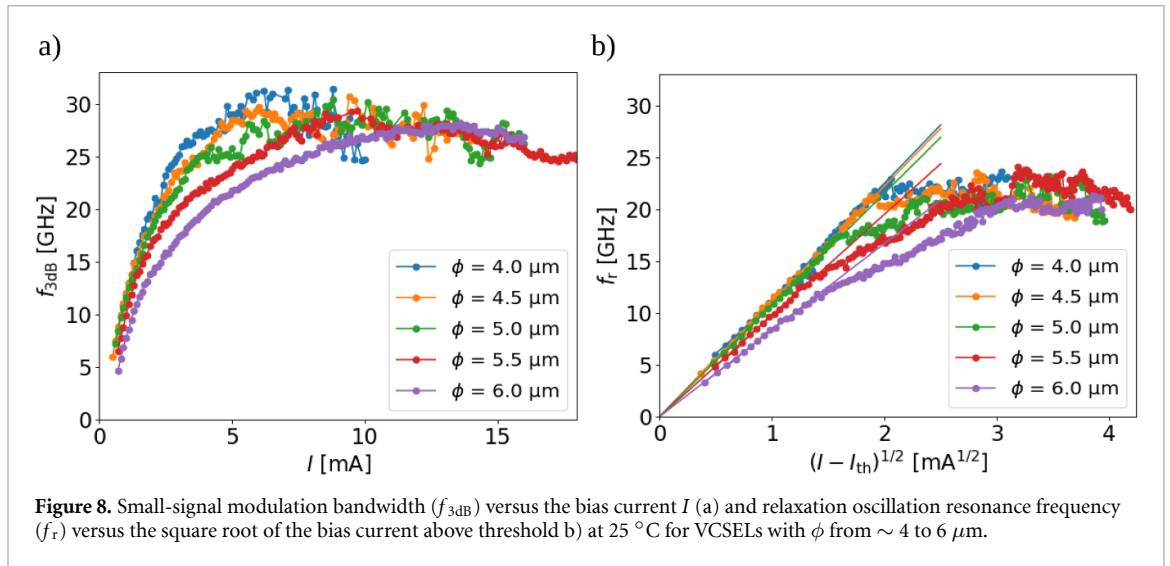


Figure 8. Small-signal modulation bandwidth (f_{3dB}) versus the bias current I (a) and relaxation oscillation resonance frequency (f_r) versus the square root of the bias current above threshold (b) at 25 °C for VCSELs with ϕ from ~ 4 to 6 μm .

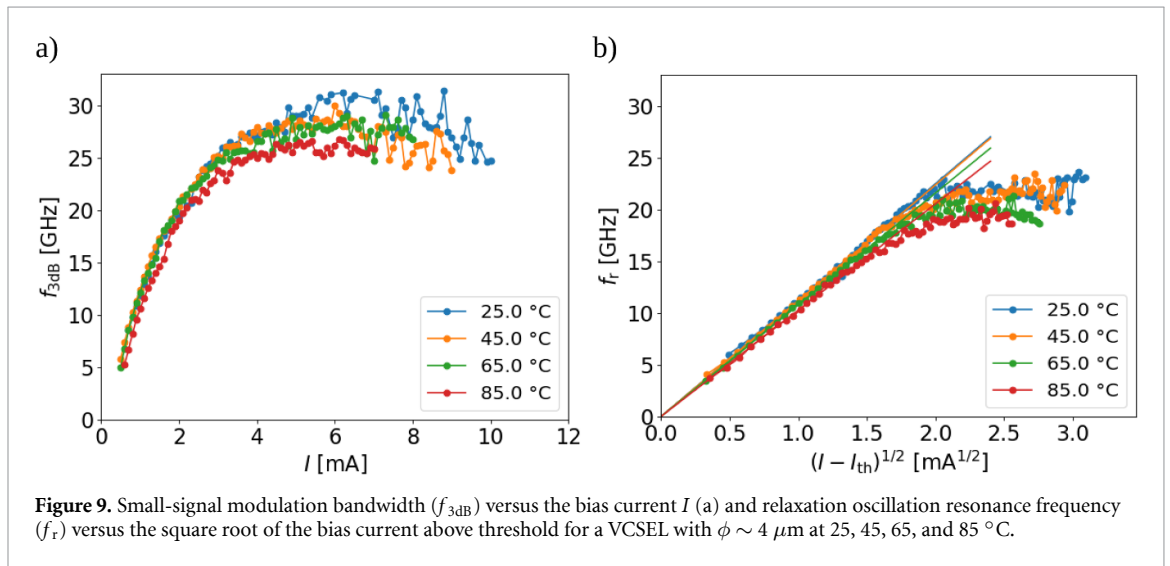


Figure 9. Small-signal modulation bandwidth (f_{3dB}) versus the bias current I (a) and relaxation oscillation resonance frequency (f_r) versus the square root of the bias current above threshold for a VCSEL with $\phi \sim 4 \mu\text{m}$ at 25, 45, 65, and 85 °C.

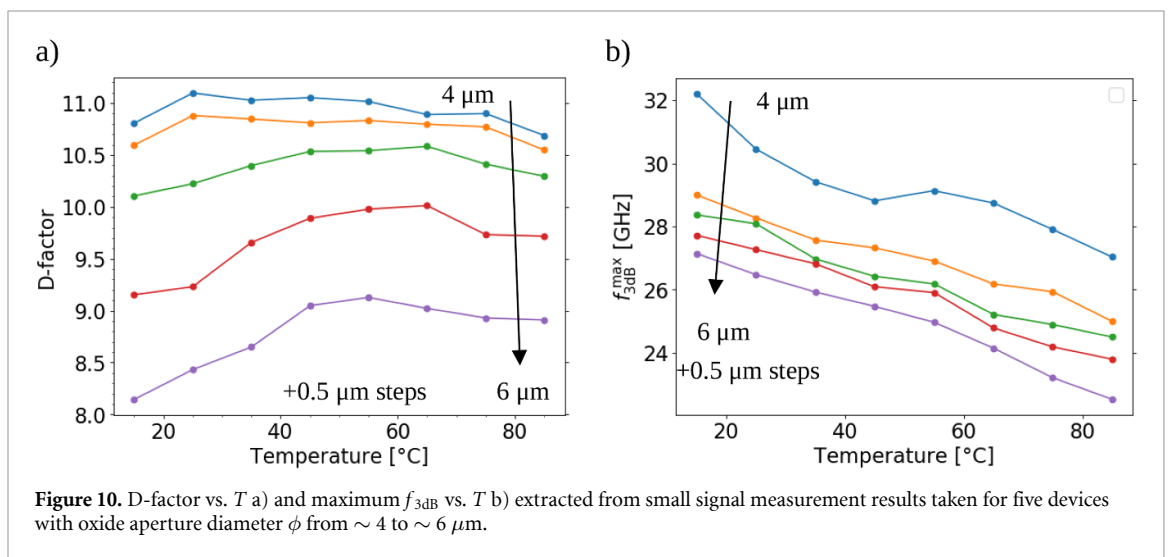
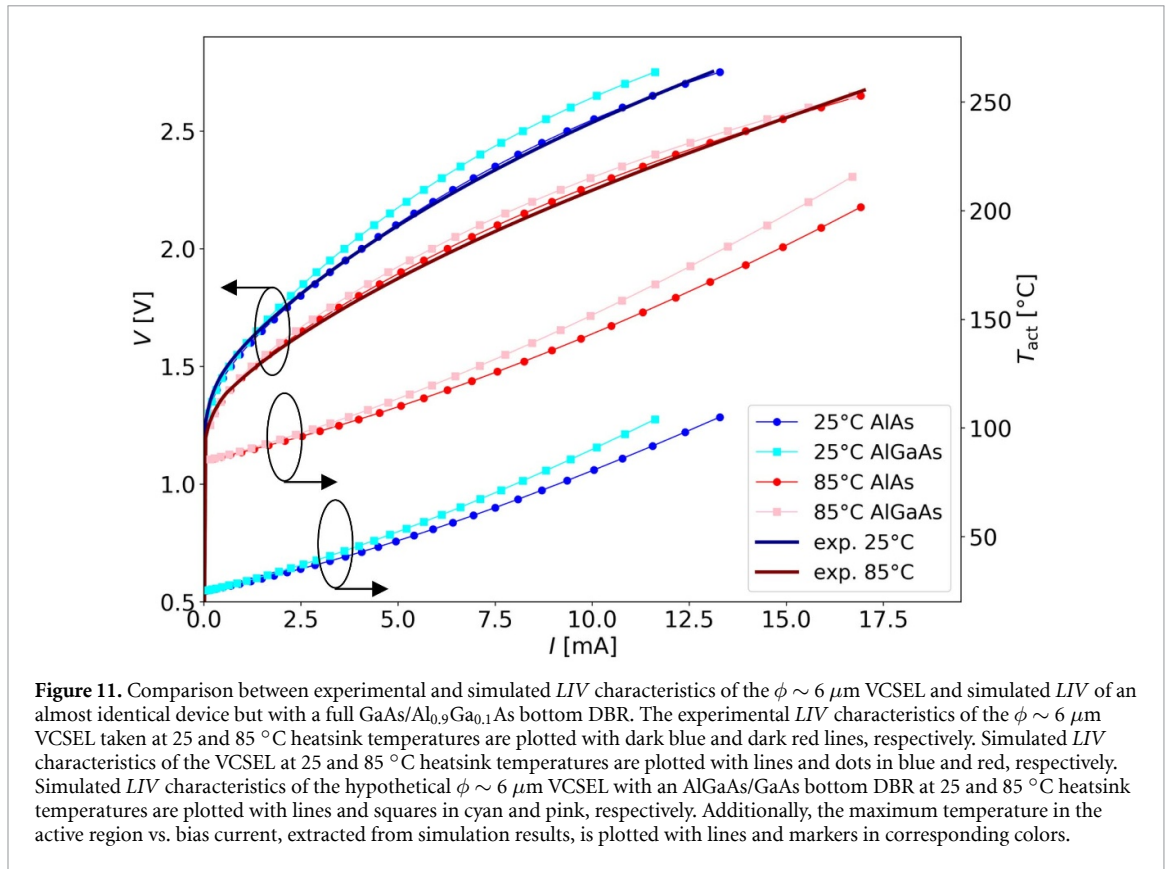


Figure 10. D-factor vs. T (a) and maximum f_{3dB} vs. T (b) extracted from small signal measurement results taken for five devices with oxide aperture diameter ϕ from ~ 4 to $\sim 6 \mu\text{m}$.

temperatures while the larger oxide aperture diameter devices tend to have the D-factor maxima at higher heat-sink temperatures.

In the figure 10(b) the maximal f_{3dB} vs. the heatsink temperature is presented. At 15 °C the maximal f_{3dB} changes from ~ 32 to ~ 27 GHz for the $\phi \sim 4$ to 6 μm VCSELs, respectively, and tends to drop with



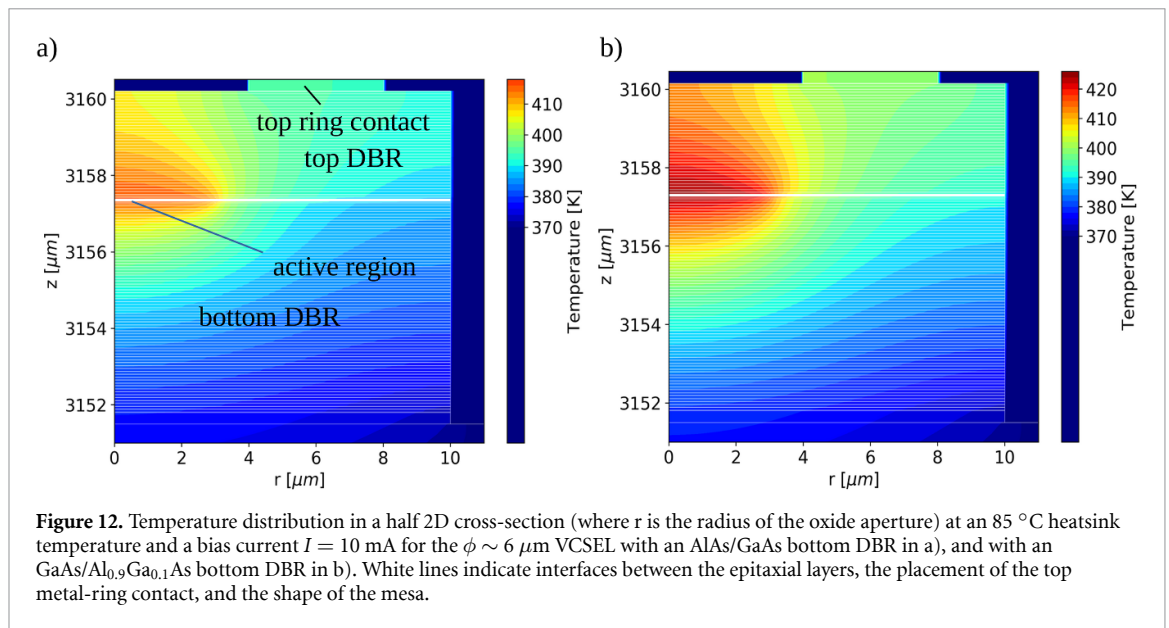
temperature for all five devices. At 85 °C the maximal $f_{3\text{dB}}$ changes from ~ 27 to ~ 22.5 GHz for the $\phi \sim 4$ to $6 \mu\text{m}$ VCSELs, respectively. The average decrease of the $f_{3\text{dB}}$ from 15 to 85 °C for all five devices is only 15%.

3.3. Simulations

To compare the performance of our VCSELs (with a hybrid 3-period GaAs/Al_{0.9}Ga_{0.1}As plus a 33-period AlAs/GaAs bottom DBR mirror) with almost identical devices but with a 36-period GaAs/Al_{0.9}Ga_{0.1}As bottom DBR mirror we perform computer simulations of the static characteristics of the devices. We use the PLaSK simulation toolkit empowered by the self-consistent, thermal-electrical-optical model of a VCSEL based on the finite-element method, developed in the Photonics Group at the Lodz University of Technology [28–33]. In the first step, parameters of the junction and averaged electrical conductivity of the p-type DBR together with their dependencies on temperature are extracted from the results of LIV measurements of the $\phi \sim 6 \mu\text{m}$ VCSEL. Other electrical and thermal parameters and their dependencies on temperature such as the electrical conductivities of the n-type GaAs and AlGaAs materials and the thermal conductivities of all the materials used are taken from the literature [34–45].

In the next step, we perform a comparison between the experimental and the simulation results for $\phi \sim 4$ to $6 \mu\text{m}$ VCSELs taken at different temperatures from 15 to 85 °C to validate the model. An example of such a comparison is presented in figure 11(a). Apart from a very good agreement between the simulated and the measured shapes of the IV curves (blue circles with a dark blue line, and red circles with a dark red line), we achieve good agreement—in the temperature in the active region—between the simulation and the values extracted from optical emission measurements. For example, the position of the fundamental mode (LP01 mode) of the $\phi \sim 6 \mu\text{m}$ VCSEL measured at 85 °C red-shifts from 989.43 nm to 992.16 nm with a change in bias current from 1 to 10 mA. Assuming the red-shift of the VCSEL cavity is 0.04 nm K^{-1} and the temperature of the active region at 1 mA is equal to the temperature of the heatsink ($\sim 360 \text{ K}$) we calculate the temperature in the active region at 10 mA is $\sim 426 \text{ K}$ which is 10 K higher than the value obtained from the simulation.

In the final step we perform simulations of a hypothetical $\phi \sim 6 \mu\text{m}$ VCSEL with a 36-period GaAs/Al_{0.9}Ga_{0.1}As bottom DBR mirror in different temperatures and compare its characteristics with the real device. As can be clearly seen in figure 11(a), the device with an GaAs/Al_{0.9}Ga_{0.1}As bottom DBR mirror is characterized by higher voltages for the same bias currents (higher differential resistance) and higher maximal temperatures in the active region in comparison to the device with an AlAs/GaAs bottom DBR mirror. The elevated maximum temperature in the active region is a result of the higher thermal resistance of



the bottom DBR which comes from the lower thermal conductivity of the Al_{0.9}Ga_{0.1}As as compared to AlAs. The temperature is higher—not only in the active region—but also in the entire device as can be seen in figure 12. This gives rise to a higher VCSEL differential resistance via a decrease of conductivity (of the hypothetical VCSEL compared to our actual hybrid DBR VCSEL) of the n-type DBR with temperature.

The elevated temperature in the active region results in a larger change in the output wavelength and a higher etalon-to-gain wavelength detuning as the bias current is increased at both 25 and 85°C heatsink temperatures. Both the etalon-to-gain wavelength detuning and the elevated VCSEL temperature have a negative impact on the overall gain in the active region. This leads to lower optical output powers at higher heatsink temperatures and larger bias currents. Additionally, a higher differential resistance (of the hypothetical VCSEL compared to our actual hybrid DBR VCSEL) negatively impacts the VCSEL energy efficiency.

4. Summary and conclusions

We presented our experimental results on top-emitting, oxide-confined 980 nm VCSELs designed to serve as optical sources for short-reach optical interconnects. The devices use a combined binary GaAs/AlAs and binary/ternary GaAs/Al_{0.9}Ga_{0.1}As bottom DBR. Increased heatsinking from incorporation of the GaAs/AlAs DBRs resulted in high temperature stability in both the static and dynamic properties of the devices and enabled measurement of a record high $\sim 27\text{ GHz}$ bandwidth at 85°C for our $\phi \sim 4\ \mu\text{m}$ VCSEL. The optical output power and the threshold current averaged for all five analyzed sizes of VCSEL apertures decreased by $\sim 40\%$ and increased by $\sim 7\%$ with a temperature increase from 15 to 85°C , respectively. All the other major static figures-of-merit, namely the maximum WPE, the WPE at LI rollover, the dR at the maximum WPE, and the R_{th} decreased by $\sim 10\%$, decreased by $\sim 2\%$, decreased by $\sim 20\%$, and increased by $\sim 20\%$ with temperature increase from 15 to 85°C , respectively. As for the dynamic properties, the average bandwidth and the average D-factor decrease by $\sim 15\%$ and increase by $\sim 3\%$ with a temperature increase from 15 to 85°C , respectively. The aforementioned parameters were obtained for relatively small devices with oxide aperture diameters from $\phi \sim 4$ to $\phi \sim 6\ \mu\text{m}$ and corresponding top mesa diameters from ~ 18 to $\sim 20\ \mu\text{m}$, respectively which normally are more influenced by temperature effects than larger devices.

The results of our self consistent thermal-electrical simulations indicate a better heatsinking of heat generated in the active region due to the use of the AlAs/GaAs bottom DBR section in comparison to a full AlGaAs/GaAs bottom DBR. Through the increased heatsinking the temperature increase in the device for bias currents from threshold to rollover is diminished. The second important feature of our structure is the decreased number of top (output coupling) DBR pairs in comparison to the typically used $20+$ pairs—resulting in a reduced photon lifetime in the cavity [22]. That in consequence leads to an increase of the $f_{3\text{dB}}$ bandwidth for all heatsink temperatures and oxide aperture diameters. The third important feature is the negative etalon-to-gain detuning which shifts the optimal working point of the VCSELs towards elevated temperatures. Through the aforementioned modifications of our epitaxial structure we are able to achieve state-of-the-art VCSEL attributes at low (close to RT) temperatures and

simultaneously similar operational figures-of-merit at elevated temperatures up to 85 °C. We achieve this result despite our use of a simplified VCSEL epitaxial design with respect to our previously published epitaxial designs and at no extra wafer processing cost.

5. Supplement A

The standard single-mode laser diode rate-equations model [27] describes a change of the photon density in a laser diode cavity and carrier density in the laser diode active region, all as functions of time. Assuming that the modulation is a sinusoidal voltage variation and the change of photon density and carrier density is very small with respect to the continuous wave (CW) values of these quantities, the parameters can be expressed via a two-pole transfer function $H(f)$ whose magnitude is defined as:

$$|H(f)|^2 = \frac{f_r^4}{(f_r^2 - f^2)^2 + \left(\frac{\gamma f}{2\pi}\right)^2} \cdot \frac{1}{1 + \left(\frac{f}{f_r}\right)^2}$$

where f_r is the relaxation oscillation resonance frequency, f is the modulation frequency, and γ is the damping. The $H(f)$ is measured via a standard small-signal measurement experiment. In this experiment, a VCSEL is driven with a modulated small amplitude sinusoidal signal at a working point set by a desired DC bias current. Since the modulation amplitude is small in comparison to the DC part of the signal, it is assumed that the conditions at which the VCSEL operates are only a function of the DC part of the current and the assumptions for the rate equation model described above are met. The heart of the measurement system is a Hewlett-Packard 8722 C vector network analyzer (VNA). The DC part of the signal is provided by a current and voltage source and fed to the VNA by a bias-tee. A VCSEL is connected to the port 1 of the VNA through a ground-signal-ground (GSG) probe and a radio frequency (RF) transmission line. A New Focus Model 1434 InGaAs photodetector module with a bandwidth of ~ 25 GHz is connected to the VNA at the port 2. The optical output signal of a VCSEL is collected by a standard OM1 silica multi-mode optical fiber with a core diameter of 62.5 μm and directed into the photodiode module. The VNA measures the real and imaginary parts of the S_{21} scattering parameter response of the system and we may plot the magnitude $|S_{21}|$ as:

$$|S_{21}| = c + 20 \cdot \log(|H(f)|) \text{ (dB)}$$

in the range from 50 Hz to 40 GHz, where c (in dB) is a constant used to set the response to 0 at 0 Hz. By fitting the results of the magnitude $|S_{21}|$ measurements the relaxation resonance frequency f_r and damping γ can be extracted. Additionally, the -3dB small-signal modulation bandwidth $f_{3\text{dB}}$ defined as the frequency for which the amplitude of the $|S_{21}|$ signal falls from its initial value by 3 dB can be evaluated. The $f_{3\text{dB}}$ bandwidth is a figure-of-merit for high speed VCSELs since the VCSEL's ability to transmit optical information is described by a bit rate (BR) which via the Shannon-Hartley Theorem is related to the $f_{3\text{dB}}$:

$$\text{BR} = \eta \cdot f_{3\text{dB}}$$

where η is the spectral efficiency in units of bits which is typically a constant for a given measurement system set up. Several assumptions and observations [27] allow us to set parameters extracted from the $|S_{21}|$ curves to the parameters inherent to a typical VCSEL, which are the D- and K-factors (D and K respectively), and the modulation-current efficiency factor (MCEF) defined as:

$$f_r = D\sqrt{(I - I_{\text{th}})}$$

$$\gamma = Kf_r^2 + \gamma_0$$

$$f_{3\text{dB}} = \text{MCEF}\sqrt{(I - I_{\text{th}})}$$

where I_{th} is the threshold current and γ_0 is the damping offset. The D-factor and the MCEF are the rates at which the f_r and $f_{3\text{dB}}$ respectively increase with bias current. Hence, high D-factor and MCEF are highly desirable in order to reach high modulation speed at low bias currents. The K-factor is a measure of damping. Low K-factors result in more pronounced resonance peaks and higher f_r and $f_{3\text{dB}}$. On the other hand, too low a K-factor may lead to higher noise, overshoot, and jitter in data transmission [46]. All three parameters D , K , and MCEF are evaluated at low bias currents, where the thermal effects have negligible impact on the VCSEL's performance. The measured $|S_{21}|$ curves are fitted to the $H(f)$ response function taking into account the photodetector response.

Acknowledgments

The German Research Foundation supports this work via the Collaborative Research Center (Sonderforschungsbereich) 787. M Gębski would like to acknowledge support from the Polish National Science Centre PRELUDIUM grant 2013/11/N/ST7/02826.

References

- [1] Schultz J 2019 How much data is created on the Internet each day? (<https://blog.microfocus.com/how-much-data-is-created-on-the-internet-each-day/#>) (accessed November 2019)
- [2] Jones N 2018 The information factories *Nature* **561** 163
- [3] Loesche D 2018 Most hyperscale data centers are operating in the U.S. (<https://www.statista.com/chart/13648/hyperscale-data-center-locations-by-country/>) (accessed November 2019)
- [4] Top 500 the list (<https://www.top500.org/lists/2019/06/>) (accessed November 2019)
- [5] Miller D A B Attojoule optoelectronics for low-energy information processing and communications *J. Lightwave Technol.* **35** 346–96
- [6] Shehabi A et al United States data center energy usage report (<https://eta.lbl.gov/publications/united-states-data-center-energy>) (accessed November 2019)
- [7] Fehrenbacher K 2016 Data centers are no longer the energy hogs they once were (<https://fortune.com/2016/06/27/data-center-energy-report/>) (accessed November 2019)
- [8] Danilak R 2017 Why energy is a big and rapidly growing problem for data centers (<https://www.forbes.com/sites/forbestechcouncil/2017/12/15/why-energy-is-a-big-and-rapidly-growing-problem-for-data-centers/#799f24015a30>) (accessed November 2019)
- [9] Miller D A B 2009 Device requirements for optical interconnects to silicon chips *Proc. IEEE* **97** 1166–85
- [10] Westbergh P, Haglund E P, Haglund E, Safaisini R, Gustavsson J S and Larsson A 2013 High-speed 850 nm VCSELs operating error free up to 57 Gbit/s *Electron. Lett.* **49** 1021–3
- [11] Haglund E, Westbergh P, Gustavsson J S, Haglund E P, Larsson A, Geen M and Joel A 2015 30 GHz bandwidth 850 nm VCSEL with sub-100 fJ/bit energy dissipation at 25–50 Gbit/s *Electron. Lett.* **51** 1096–8
- [12] Liu M, Wang C Y, Feng M and Holonyak N Jr. 2016 850 nm oxide-confined VCSELs with 50 Gb/s error-free transmission operating up to 85 °C *Conf. on Lasers and Electro-Optics* pp SF1L–6
- [13] Kuchta D M et al 2012 A 55 Gb/s directly modulated 850 nm VCSEL-based optical link *IEEE Photonics Conf.* pp PD1–5
- [14] Kuchta D M et al 2013A 56.1 Gb/s NRZ modulated 850 nm VCSEL-based optical link *Optical Fiber Communication Conf.* pp OW1B–5
- [15] Liu M, Wang C Y, Feng M and Holonyak N Jr. 2016 50 Gb/s error-free data transmission of 850 nm oxide-confined VCSELs *Optical Fiber Communication Conf.* pp Tu3D–2
- [16] Kuchta D M, Ryljakov A V, Doany F E, Schow C L, Proesel J E, Baks C W, Westbergh P, Gustavsson J S and Larsson A 2015 A 71-Gb/s NRZ modulated 850-nm VCSEL-based optical link *IEEE Photon. Technol. Lett.* **27** 577–80
- [17] Kuchta D M, Ryljakov A V, Schow C L, Proesel J E, Baks C W, Westbergh P, Gustavsson J S and Larsson A 2015 A 50 Gb/s NRZ modulated 850 nm VCSEL transmitter operating error free to 90 °C *J. Lightwave Technol.* **33** 802–10
- [18] Moser P, Lott J A and Bimberg D 2013 Energy efficiency of directly modulated oxide-confined high bit rate 850-nm VCSELs for optical interconnects *IEEE J. Sel. Top. Quantum Electron.* **19** 1702212
- [19] Li H et al 2015 Temperature-stable, energy-efficient, and high-bit rate oxide-confined 980-nm VCSELs for optical interconnects *IEEE J. Sel. Top. Quantum Electron.* **21** 1700409
- [20] Li H, Wolf P, Moser P, Larisch G, Lott J A and Bimberg D 2014 Temperature-stable 980-nm VCSELs for 35-Gb/s operation at 85 °C with 139-fJ/bit dissipated heat *IEEE Photonics Technol. Lett.* **26** 2349–52
- [21] Moser P, Larisch G, Li H, Moser P, Wolf P and Lott J A 2014 Error-free 46 Gbit/s operation of oxide-confined 980 nm VCSELs at 85 °C *Electron. Lett.* **50** 1369–71
- [22] Śpiewak P et al 2018 Impact of the top DBR in GaAs-based VCSELs on the threshold current and the cavity photon lifetime *Proc. SPIE 10552, Vertical-Cavity Surface-Emitting Lasers XXII* p 105520O
- [23] Rosales R, Zorn M and Lott J A 2017 30-GHz Bandwidth with directly current-modulated 980-nm oxide-aperture VCSELs *IEEE Photonics Technol. Lett.* **29** 2107–10
- [24] Haghghi N, Moser P and Lott J A 2019 Power, bandwidth, and efficiency of single VCSELs and small VCSEL arrays *IEEE J. Sel. Top. Quantum Electron.* **25** 495–502
- [25] Haghghi N et al 2018 35 GHz bandwidth with directly current modulated 980 nm oxide aperture single cavity VCSELs *IEEE Int. Semiconductor Laser Conf. (ISLC)* p WD4
- [26] Liu A, Wolf P, Lott J A and Bimberg D 2019 Vertical-cavity surface-emitting lasers for data communication and sensing *Photonics Res.* **7** 121–36
- [27] Coldren L A, Corzine S W and Mašanović M L 2012 *Diode Lasers and Photonic Integrated Circuits* 2nd edn (New York: Wiley)
- [28] Czyszanowski T, Sarzała R P, Dems M, Walczak J, Wasiak M, Nakwaski W, Iakovlev V, Volet N and Kapon E 2013 Spatial-mode discrimination in guided and antiguided arrays of long-wavelength VCSELs *IEEE J. Sel. Top. Quantum Electron.* **19** 13487855
- [29] Wasiak M, Śpiewak P, Moser P, Walczak J, Sarzała R P, Czyszanowski T and Lott J A 2016 Numerical model of capacitance in vertical-cavity surface-emitting lasers *J. Phys. D: Appl. Phys.* **49** 175104
- [30] Sarzała R P, Marciniak M and Czyszanowski T 2018 Thermal properties of GaN-based semiconductor-metal subwavelength grating VCSELs and novel current injection scheme,” *J. Phys. D: Appl. Phys.* **51** 285102
- [31] Sarzała R P, Czyszanowski T and Nakwaski W 2014 Effect of relief aperture on single-fundamental-mode emission of 1.3- μm GaInNAs GaAs-based VCSELs *IEEE J. Quantum Electron.* **50** 874–81
- [32] Wasiak M 2011 Mathematical rigorous approach to simulate an over-threshold VCSEL operation *Physica E* **43** 1439–44
- [33] Gębski M, Dems M, Lott J A M and Czyszanowski T 2015 Monolithic subwavelength high-index-contrast grating VCSEL *IEEE Photon. Technol. Lett.* **27** 1953–6

- [34] Mollenkamp L W, Eppenga R, Hooft G W, Dawson P, Fozon C T and Moore K J 1980 Determination of valence-band effective-mass anisotropy in GaAs quantum wells by optical spectroscopy *Phys. Rev. B* **38** 4314–7
- [35] Springthorpe A J, King F D and Becke A 1975 Te and Ge-doping studies in Ga/sub 1-x/Al/sub x/As *J. Electron. Mater.* **4** 101–18
- [36] Nakwaski W and Osiński M 1993 Thermal analysis of GaAs-AlGaAs etched-well surface-emitting double-heterostructure lasers with dielectric mirrors *IEEE J. Quantum Electron.* **29** 1981–95
- [37] Swaminathan V, Zilko J L, Tang W T and Wagner W R 1982 Photoluminescence study of acceptors in Al_xGa_{1-x}As *J. Appl. Phys.* **53** 5163–8
- [38] Nakwaski W 1992 Hole mobility in carbon-doped GaAs and (AlGa)As *Phys. Status Solidi A* **132** K47–K49
- [39] Saxena A K and Gurumurthy K S 1982 Scattering parameters from an analysis of the Hall electron mobility in Ga_{1-x}Al_xAs alloys *J. Phys. Chem. Solids* **43** 801–8
- [40] Sun S Z, Armour E A, Zheng K and Schaus C F 1991 Zinc and tellurium doping in GaAs and Al_xGa_{1-x}As grown by MOCVD *J. Cryst. Growth* **113** 103–12
- [41] Masu K, Konagai M and Takahashi K 1980 Acceptor energy level for Zn in Ga_{1-x}Al_xAs *J. Appl. Phys.* **51** 1060–4
- [42] Ayabe M, Mori Y and Watanabe N 1981 An Anomaly in the relation of hall coefficient to resistivity in n-type Al_xGa_{1-x}As *Jpn. J. Appl. Phys.* **20** L55–L58
- [43] Fehse R, Tomić S, Adams A R, Sweeney S J, O'Reilly E P, Andreev A and Riechert H 2002 A quantitative study of radiative, Auger and defect-related recombination processes in 1.3 μm GaInNAs-based quantum-well lasers *IEEE J. Sel. Top. Quantum Electron.* **8** 801–10
- [44] Adachi S 1985 GaAs, AlAs, and Al_xGa_{1-x}As Material parameters for use in research and device applications *J. Appl. Phys.* **58** R1–R29
- [45] Amith A, Kudman I and Steigmeier E F 1965 Electron and phonon scattering in GaAs at high temperatures *Phys. Rev.* **138** A1270–A1276
- [46] Haglund E 2015 VCSELs for high-speed, long-reach, and wavelength-multiplexed optical interconnects *Dissertation for the Degree of Doctor of Philosophy* Chalmers University of Technology Göteborg